Turbulent Flow over Thin Rectangular Riblets

O. A. El-Samni
Mechanical power Engineering Department, The University of Alexandria, El-Chatby, Alexandria 21411, Egypt
Hyun Sik Yoon*, Ho Hwan Chun
Advanced Ship Engineering Research Center (ASERC), Pusan National University, San 30, Jangjeon-dong, Geumjeong-gu, Busan 609-735, Korea

The effect of longitudinal thin rectangular riblets aligned with the flow direction on turbulent channel flow has been investigated using direct numerical simulation. The thin riblets have been modeled using the immersed boundary method (IBM) where the velocities at only one set of vertical nodes at the riblets positions are enforced to be zeros. Different spacings, ranging between 11 and 43 wall units, have been simulated aiming at getting the optimum spacing corresponding to the maximum drag reduction while keeping the height/spacing ratio at 0.5. Reynolds number based on the friction velocity u_τ and the channel half depth δ is set to 150. The flow is driven by adjusted pressure gradient so that the mass flow rate is kept constant in all the simulations. This study shows similar trend of the drag ratio to that of the experiments at the different spacings. Also, this research provides an optimum spacing of around 17 wall units leading to maximum drag reduction as experimental data. Explanation of drag increasing/decreasing mechanism is highlighted.

Key Words: Drag Reduction, Riblets, Turbulent Channel Flow, DNS, IBM, Flow Control

Nomenclature

k : Turbulent kinetic energy
p : Pressure
r_z : Spanwise separation
Re_τ : Friction Reynolds number, $\mathrm{Re}_\tau = u_\tau \delta / \nu$
R_{ii} : Two-point correlations
t : Time
T : Thickness of riblet
U_i, u_i : Mean and instantaneous velocity component in i^{th} direction
u_τ : Friction velocity, $\sqrt{\tau_w/\rho}$
u_τ^* : Friction velocity estimated from the total mean velocity
x, y, z : Streamwise, wall-normal and spanwise directions
δ : Channel half width
δ_{ij} : Kronecker delta
ν : Kinematic viscosity
ρ : Density
τ : Wall shear stress
H : Height of riblet
S : Distance between two riblets
f_i : Momentum forcing
q : Mass source/sink

Subscripts, superscripts and notations

rms : Root mean square value of the fluctuating variable
$+$: Normalized by wall variables; u_τ and ν on each wall
$-$: Average over x-z planes and time
$'$: Fluctuating quantities
W : Wall

* Corresponding Author,
E-mail : lesmodel@pusan.ac.kr
TEL : +82-51-510-3685; **FAX** : +82-51-581-3718
Advanced Ship Engineering Research Center (ASERC), Pusan National University, San 30, Jangjeon-dong, Geumjeong-gu, Busan 609-735, Korea. (Manuscript **Received** January 31, 2005; **Revised** July 22, 2005)

1. Introduction

Riblet has been known as one of the practical

methods in passive drag reduction techniques of turbulent boundary layer flows. It can thought of as wall surface with micro-grooves aligned in or titled slightly to the flow direction. The riblets work to change the small eddy structures in turbulent boundary layers by damping the lateral motion of fluids which in turns, suppress the generation and sustaining mechanism of near-wall coherent structures. Such changes may lead to an increase or decrease in friction drag depending on the relative sizes of the eddy structures to the sizes of the embedded riblets. Continuous efforts have been devoted to the development of an optimum shape of riblets aiming at attaining higher rates of drag reduction in aeronautics and hydrodynamics fields. Different shapes including the triangular, rectangular, trapezoidal, sawtooth and scalloped cross-sections have been investigated aiming at proposing the optimum shape to get the drag reduction.

Early, Walsh (1982, 1983) reported the favorable property of reducing the friction drag up to 8% in laboratory experiments. There are many researchers who have extended the knowledge about the mechanisms associated with the drag reduction analytically (Bechert and Bartenwerfer, 1989), or using numerical methods (Choi et al., 1993; Chu and Karniadakis, 1993; Goldstein et al., 1995a, 1995b; Stalio and Nobile, 2003) and experimental methods (Choi, 1989; Vukoslavcevic et al., 1992; Bruce, 1993; Suzuki and Kasagi, 1994; Bechert et al., 1997, 2000). Among the different configurations studied before, the thin rectangular riblets have shown the maximum drag reduction which amounts to 10% according to Bechert et al. (1997).

The numerical simulations have lagged the experiments during the last decades due to the difficulties in treating complex geometries numerically. Although the few numerical simulations mentioned above have well represented the global drag reduction observed by the experiments, there is still much work to do in order to simulate more complicated configurations such as the scalloped cross-sections or deformable walls. Recently, new methodologies have been developed to overcome the difficulty of generating special fitted surfaces to the complicated shapes of riblets. Among such techniques, the immersed boundary method (IBM) has shown promising results. Goldstein et al. (1995a) had presented IBM to be used in turbulent channel flow using Spectral Methods. In series of DNS, Goldstein et al. (1995b) extended the IBM to simulate different geometries of riblets and wires. The IBM has been applied to finite difference and finite volume successfully for simpler flows. Saiki and Biringen (1996); Ye et al. (1999) applied it to 2D cylinder and complex geometries using FD (finite difference).

Recently, a modified immersed boundary method was suggested by Kim et al. (2001). The momentum forcing in the Navier-Stokes equations and the mass source/sink in the continuity equation were adopted to satisfy the no-slip condition on the immersed boundary and the mass conservation for the cells intersected with the immersed boundary. Here the momentum forcing and mass source/sink are applied only on the body surface or inside the body. By applying this IBM to a second order FV code, Kim et al. (2001) successfully simulated the flow around cylinder and sphere.

In IBMs, when the obstacle is big enough to enclose more grid points inside its boundaries, the treatment of the surface would be better. To ensure zero velocity at the surface, artificial velocities inside the obstacle (at the nearest interior points) should be generated in the opposite direction to those outside the body (at the nearest exterior points). Therefore, obstacles of infinitesimal sizes less than the computational grid sizes are still challenging problem. To our knowledge, the above mentioned numerical techniques have not studied such thin riblet configurations.

The present study aims at exploring the flow above very thin riblets whose thicknesses are much less than the grid spacing. Due to the various parameters describing the geometry of the riblets (thickness, height and spacing), we selected a fixed height to spacing ratio of 0.5 and negligible thickness. The only changing parameter would be the spacing between riblets. Selecting those ratios was based on the conclusion of Bechert et al. (1997) which showed the maxi-

mum drag reduction by the various combinations of parameters in their experiments. Further studies for the effect of the riblet thickness and height to spacing ratio will be conducted. For this purpose, the IBM is implemented in order to force the velocities along only one vertical set of grids up to the height of the riblets to zeros.

2. Computational Details

Figure 1 shows the flow geometry and coordinates system. In this study, x, y and z denote the streamwise, wall-normal and spanwise directions, respectively. Also, H, T and S indicate the height, thickness of riblet and the distance between two neighboring riblets, respectively. Only the lower wall is evenly distributed with the thin riblets. No-slip and no-penetration boundary conditions are enforced at both walls. The turbulent flow is assumed fully developed over the riblets so that the periodic boundary conditions are simply assigned in the streamwise (x) and spanwise (z) directions.

The governing equations describing instantaneous incompressible viscous flow in the present study are the unsteady three-dimensional continuity, momentum equations:

$$\frac{\partial u_i}{\partial x_i}=0 \tag{1}$$

$$\frac{\partial u_i}{\partial t}+u_j\frac{\partial u_i}{\partial x_j}=-\frac{\partial p}{\partial x_i}+\frac{1}{\mathrm{Re}_\tau}\frac{\partial^2 u_i}{\partial x_j^2}+f_i \tag{2}$$

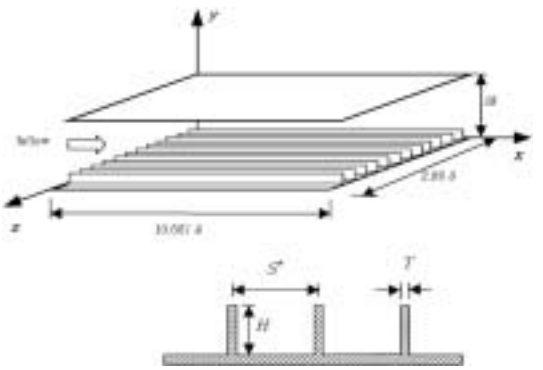

Fig. 1 Schematic of flow geometry and coordinate system

where x_i are Cartesian coordinates, u_i are the corresponding velocity components, and f_i is the momentum forcing. In order to simulate very thin riblet where the three components of velocity are to be zero at the surface, a collocated grid system has been used rather than the staggered grid used by Kim et al.(2001). The locations of velocity components coincide with the pressure nodes. The forcing f_i is obtained by the direct scheme proposed by Mohd-Yusof (1997). The time discretization of equation (2) regardless of the spatial treatments of the viscous, pressure and nonlinear terms can be written in general form as;

$$\frac{u_i^{n+1}-u_i^n}{\Delta t}=-u_j\frac{\partial u_i}{\partial x_j}-\frac{\partial p}{\partial x_i}+\frac{1}{\mathrm{Re}_\tau}\frac{\partial^2 u_i}{\partial x_j^2}+f_i \tag{3}$$

The forcing f_i needed to ensure that u_i^{n+1} is zero at the riblet nodes can be obtained by arranging equation (3) if all the other terms are known from the latest time step

$$f_i=\frac{-u_i^n}{\Delta t}+u_j\frac{\partial u_i}{\partial x_j}-\frac{\partial p}{\partial x_i}+\frac{1}{\mathrm{Re}_\tau}\frac{\partial^2 u_i}{\partial x_j^2} \tag{4}$$

Whereas f_i would be zero elsewhere in the domain.

The variables in the above equations are normalized by the channel half depth δ, friction velocity u_τ. The normalization results in one dimensionless parameter of the friction Reynolds number $\mathrm{Re}_\tau=u_\tau\delta/\nu$. Low Reynolds number of 150 is used in the present study. The driving pressure gradient is adjusted to keep constant mass flow rate in the x-direction in all simulations. As shown in Fig. 1, the computational domain has the dimensions $10.667\delta\times2\delta\times2.88\delta$ in x-, y- and z-directions, respectively. Spacing (S) has been changed from around 11 to 43 wall units.

The central difference scheme with the second-order accuracy based on the finite volume method is used for the spatial discretization. The collocated grid system is used to facilitate the imposing of the forcing on vertical line of grids. The control volume faces are centered between the velocity nodes. A two-step time-split scheme is

used to advance the flow field which is based on the previous works of Kim and Moin (1985); Zang et al.(1994).

First the velocity is advanced from time level 'n' to an intermediate level '$*$' by solving the advection-diffusion equation without pressure term. In the advection-diffusion step, the non-linear terms are treated explicitly using third-order Adams-Bashforth scheme. The diffusion terms are treated implicitly using Crank-Nicolson scheme. The semi-discrete advection-diffusion equation including momentum forcing f_i is

$$\frac{u_i^*-u_i^n}{\Delta t}+\left[\frac{23}{12}\frac{\partial}{\partial x_j}(u_ju_i)^n-\frac{16}{12}\frac{\partial}{\partial x_j}(u_ju_i)^{n-1}+\frac{5}{12}\frac{\partial}{\partial x_j}(u_ju_i)^{n-2}\right] \tag{5}$$
$$=\frac{1}{\mathrm{Re}_\tau}\left[\frac{1}{2}\left(\frac{\partial^2 u_i^n}{\partial x_j^2}+\frac{\partial^2 u_i^*}{\partial x_j^2}\right)\right]+f_i^n$$

Then the following Poisson equation, which is derived by using mass conservation, for pressure is solved fully implicitly.

$$\frac{\partial^2 p^{n+1}}{\partial x_j^2}=\frac{1}{\Delta t}\left(\frac{\partial u_j^*}{\partial x_j}\right) \tag{6}$$

Once the pressure is obtained, the velocity field at '$n+1$' is obtained with a pressure-correction step.

$$u_i^{n+1}=u_i^*-\Delta t\left(\frac{\partial p^{n+1}}{\partial x_i}\right) \tag{7}$$

The pressure correction is applied at both the velocity nodes and at the control volume cell faces as well.

The simulations and the present results have used $64\times65\times144$ grid points in the streamwise, wall-normal and spanwise directions, respectively. Uniform meshes have been used in streamwise and spanwise directions while the wall-normal direction uses a hyperbolic tangent distribution to account for the high gradients near the walls. Higher resolution simulations are underway accumulating valuable statistical description of near wall alteration due to riblets.

The time step is set to $0.075\,\nu/u_\tau^2$ in order to keep the CFL number below 0.3. The flow reaches the fully developed state after nearly 2000 ν/u_τ^2. Plane averages over x-z planes and time have been accumulated for non-dimensional time interval of 3000 ν/u_τ^2 which is quite longer than the periods used in generating databases in the other DNS simulations of channel flows over riblets.

3. Results and Discussions

Figure 2 shows the comparison of the drag reduction rate $\Delta\tau/\tau_0$ obtained in the present study with the experimental data of Bechert et al.(1997) for different spacing S^+. Here, S^+ is defined as $S^+=Su_\tau/\nu$, and u_τ is calculated from the τ at the riblet surface. The shear stress on the flat plate τ_0 is calculated from independent simulation at the same Reynolds number, thus $\Delta\tau=\tau-\tau_0$ is the difference of the shear stresses between riblet plate and flat plate. Since the shear stress at the upper non-riblet surface can be estimated directly from the mean velocity gradient, the shear stress at the riblet surface can be deduced from the momentum balance in the flow direction. Negative and positive value of $\Delta\tau/\tau_0$ represents the drag reduction and increase, respectively. As shown in Fig. 2, the profiles of plane and time-averaged shear stress rates as function of the lateral riblet spacing show quali-

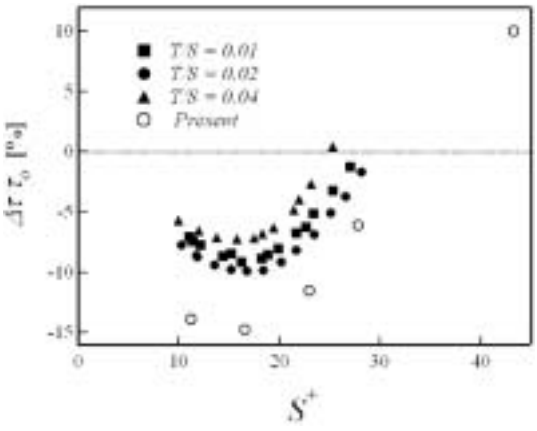

Fig. 2 Drag reduction rate as a function of riblet spacing obtained by present simulation, which is compared with that of the experiments of Bechert et al.(1997)

tatively good agreement with the experimental data of Bechert et al.(1997). The optimum value of riblet spacing obtaining the maximum drag reduction can be found from both results. This optimum value is about 17 wall unit, where the maximum drag of 15% obtained from the present study is higher than the experimental measurements of Bechert et al.(1997) corresponding to 7% for $T/S=0.04$, 9% for $T/S=0.01$ and 10% for $T/S=0.02$. Also present study shows that larger S^+ can lead to drag reduction in the limit for $S^+<35$. But, the experiments show lower spacing of $S^+<30$ at which the net drag is zero as shown in Fig. 2.

It worth mentioning that the experiments of Bechert et al.(1997) had been done for ranging between 250 to 700. They mentioned that their drag reduction data at lower Reynolds number than 250 had deviated from that at higher Reynolds number experiments. Therefore the relative deviation between the drag reduction rates in present results and Bechert et al.(1997) can be partially contributed to the effect of low Reynolds number and also to the thickness of the riblets. Since the wetted area of the riblets would be theoretically the minimum when the thickness is zero, one can expect that the drag reduction rate will be lower than that of Bechert et al. (1997).

To clarify the effect of thickness, the present authors (El-Samni et al., 2005) have used Cartesian Grid Method for thickness/spacing ratio of 0.02 and obtained drag reduction ratio of 11% which is much closer to experiments of Bechert et al.(1997) than present IBM result.

Two kind of averaging of profiles are used. Averaging over the riblets tip is performed along all the vertical x-y planes passing through the riblets and averaging over the valleys is done by summing all planes lying between the riblets positions. The later average may mislead readers since it smears the variation of velocities and Reynolds stresses within the distance between two adjacent riblets. In other words, values at the central plane of the valley differ significantly from those at the adjacent plane next to the riblet surface.

Figure 3 shows the variation of streamwise mean velocity in global units for the different riblet spacing. The streamwise velocities averaged over x-z planes are revealed in Fig. 3(a). Otherwise, Fig. 3(b) shows the streamwise velocities averaged over x-z planes corresponding to riblet tips. As riblet spacing, S^+ increases, mean velocity becomes smaller in near riblet side for $\delta/\delta \leq -0.75$. In contrast, from $y/\delta > -0.75$ to $y/\delta \approx 0.85$ the mean velocity becomes lager with S^+ increasing in order to compensate the velocity reduction in riblet side, because present simulations are carried out by fixing mass flow rate in the x-direction. No apparent variation of the mean velocity is found above $y/\delta \approx 0.85$ accord-

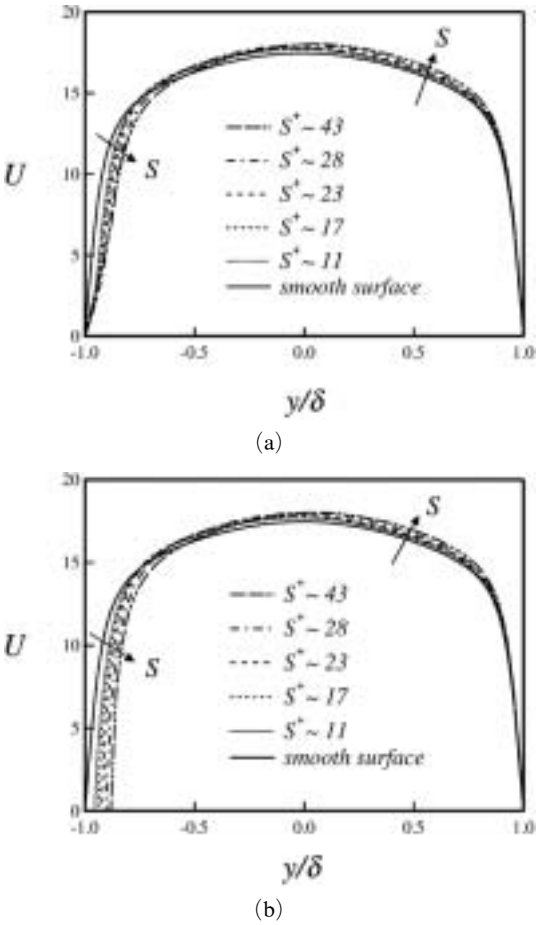

Fig. 3 (a) Total mean streamwise velocity and (b) mean streamwise velocity above riblet tips in global units for different riblet spacings

ing to different riblet spacing. The mean velocity is almost same along the spanwise direction except near the riblets. Also, the mean velocity above the riblet spacing is larger than that above the riblet tip at any given location of y. These results have been observed in previous researches (Choi et al., 1993; Bechert and Bartenwerfer, 1989; Vukoslavcevic et al., 1992).

Mean velocity profiles normalized by the inner values at each wall are plotted for the different riblet spacing in Fig. 4. The profiles are shifted towards higher values of y^+ by a distance equivalent to the riblets height. However, the logarithmic region appears in both cases but it is shifted up in the drag reducing cases whereas it shows little shift downward in the drag increasing case, which indicates the increase and decrease of the boundary layer thickness in the former and the later cases, respectively (Choi et al., 1993).

RMS of Reynolds stress normal components are shown in Fig. 5 for the two most distinctive cases; drag reducing case of $S^+\sim17$, Fig. 5(a), and drag increasing case of $S^+\sim43$, Fig. 5(b). In the valley between the riblets, u_{rms} decreases more significantly in the drag reducing case. As the spacing S^+ decreases from 43 to 17 wall units, the suppression of u_{rms} in the valley region is more pronounced. Hence, it can be inferred that a layer of height H^+ works as a damping zone for the Reynolds stress and its effect becomes clearer in smaller heights. The same damping effect has been observed in both lateral components v_{rms} and w_{rms} in the valley region. However, at the widest spacing of $S^+\sim43$, v_{rms} does not show much reduction compared with that of smooth surface and the magnitude of w_{rms} is of the same order of that of v_{rms}. This may indicate the penetrating and residing of some coherent streamwise vortices in the valley between riblets especially when the spacing increases more than the nominal sizes of such vortices whose diameters were estimated by Kim et al.(1987) to be around 25 wall units. Values of v_{rms} and w_{rms} are comparable within the valleys of $S^+\sim24$ and 28 cases as well, whereas they are much

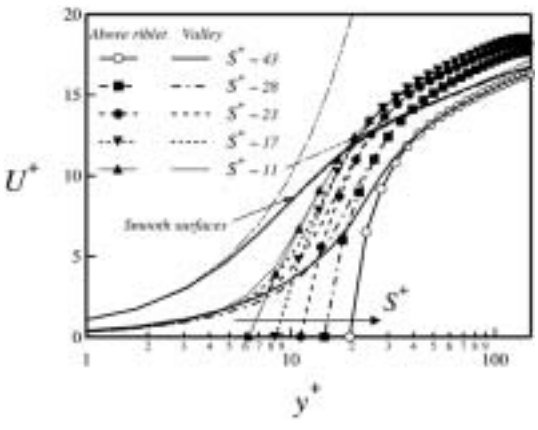

Fig. 4 Mean streamwise velocity profiles normalized by the inner wall values at each wall for different riblet spacing

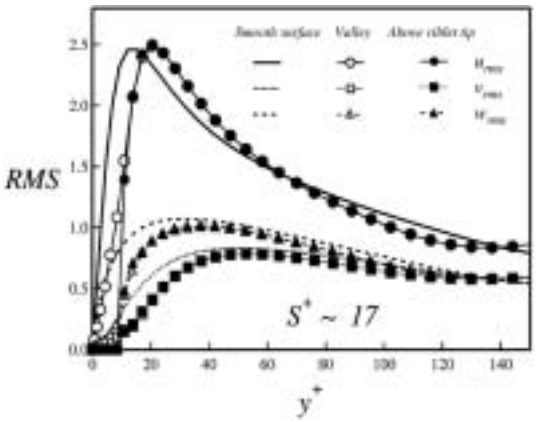

(a)

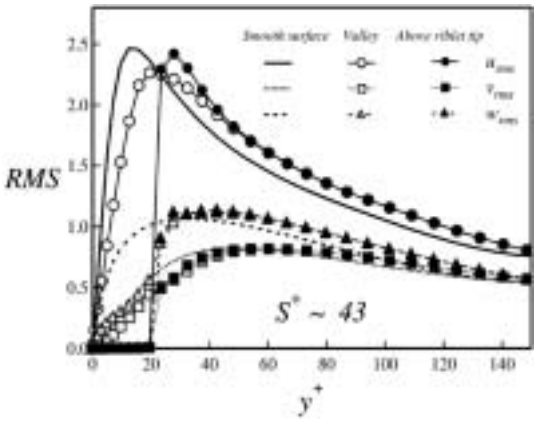

(b)

Fig. 5 RMS of Reynolds normal stresses normalized by the inner wall values at each wall for (a) for $S^+\sim17$ and (b) $S^+\sim43$ cases

suppressed in cases of $S^+\sim7$ and 12 since the riblets spacing becomes narrower enough to prevent the penetration of quasi streamwise vortices to reside in the valleys. The peak of u_{rms} is shifted towards higher y^+. While the peak is observed at $y^+\sim14$ in smooth surface simulations, it occurs at $y^+\sim23.5$ in drag increasing case $(S^+\sim43)$ and at $y^+\sim24$ in drag decreasing case $(S^+\sim17)$. Since the peak of u_{rms} is associated with the planes at which low- and high-speed streaks are more prevailing, the larger shifting of such peak in drag-reducing case indicates the blockage effect of the riblet to near-wall activities in a layer of thickness equal almost to the height of the riblets. The larger the spacing, the smaller would be the blockage effect and hence the peak of u_{rms} would be at lower distances. The lateral components of Reynolds stress v_{rms} and w_{rms} are reduced in regions above the tip level, $y^+>9$, in drag-reducing case. Both components increase slightly in the drag-increasing case for $y^+>20$, especially w_{rms}. Although the narrower riblet spacing $(S^+<20)$ shifts the streaks upward, there is less near wall activities due to the damping effect to the vertical structures in this zone. On the other hand, the widest spacing $(S^+\sim43)$ permits the vortices to reside inside the valleys and also to evolve in the region above the riblets tips.

Reynolds shear stress is plotted in Fig. 6 compared with that at smooth surface. In Fig. 6(a), the stress is suppressed according to the damping effects on the near-wall vertical structures. The value of $-\overline{u'^+v'^+}$ in the valley is almost zero whereas the profile averaged above the riblet tips collapses well with that averaged over the valley in most the channel at $y^+>9$. This indicates that the mechanism for generating $-\overline{u'^+v'^+}$ above the riblets tips is similar to that above the valley regions, which suggests again the upward shift of the streaks layer with frozen layer (with very small activity) below $y^+\sim9$. In contrast to this image, $-\overline{u'^+v'^+}$ averaged above the riblets tips has considerable peak in drag-increasing case as shown in Fig. 6(b). As it will be shown later, the wide spacing permits eddies above the riblet height region to push fluid from the high speed

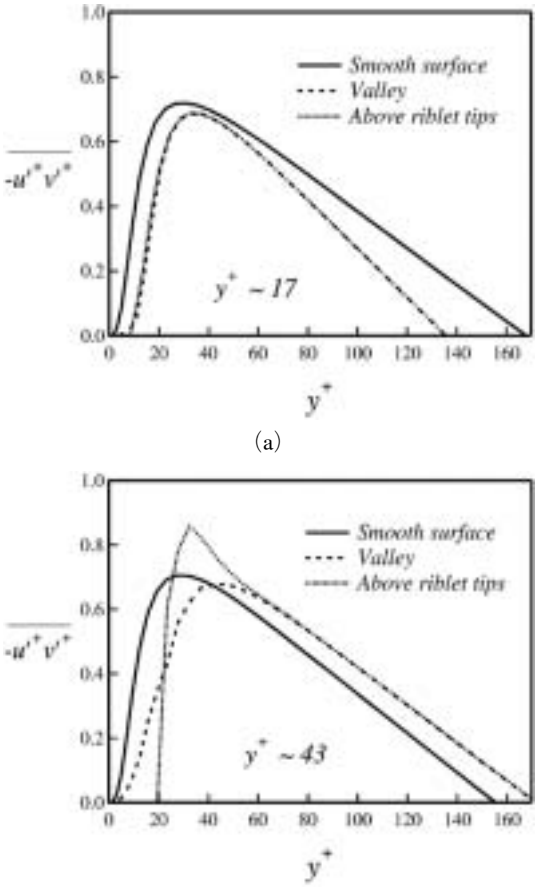

Fig. 6 Reynolds shear stress normalized by the inner wall values at each wall for (a) for $S^+\sim17$ and (b) $S^+\sim43$ cases

region into the valley which in turns forms smaller eddies inside the valley. Thus, the smaller eddies move the low speed fluid outward from the valley region passing mostly adjacent to the riblet surface. Such scenario results in larger positive v' at the riblets tips. With the retardation or the streamwise velocity, there exists a peak for $-\overline{u'+v'^+}$ in this region as shown in Fig. 6 (b) at $y^+>20$. Due to the vortices penetration inside the valleys and the out rush of fluids from the valleys nearer to the riblets, the mechanism of generating $-\overline{u'^+v'^+}$ above the riblets differs from that above the valley so that the averaged profiles depart up to $y^+\sim60$. The difference does not propagate further into the channel core.

Flow visualization of two distinctive increasing and reducing drag cases are shown in Fig. 7, where the streamwise velocity contours and the cross-stream velocity vectors are plotted. It can be observed that the case of increased drag where the spacing being larger than the nominal sizes of the quasi-streamwise coherent structures so that eddies may reside inside the valley between two adjacent riblets as seen clearly in Fig. 7(a). On the other hand, the smaller spacing elevates the rotating eddies to higher y^+ further from the wall and no penetration of the quasi-streamwise structures inside the valley between riblets. In the former case, the wetted area against which eddies are rotating increases leading to larger rates of drag.

Low and high-streaks a drag increasing and decreasing cases are shown in Fig. 8 and Fig. 9, respectively. In Fig. 8(a), the streaks in the valley of the riblets are shown where they appear aligned in the streamwise direction due to the effect of the fence of riblets. In this case, 12 fins are evenly distributed within the full spanwise length of the picture but the lines of the riblets are removed from the image to be clearer. At the position of maximum u'_{rms} shown in Fig. 8(b), the streaks of low- and high-speed reveal more intermittency and the disappearing of the meandering of the streaks. The streaks on the smooth surface at the same y^+ of maximum u'_{rms} preserve the typical meandering of 2D turbulent channel

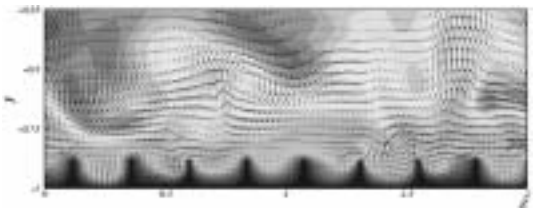

(a)

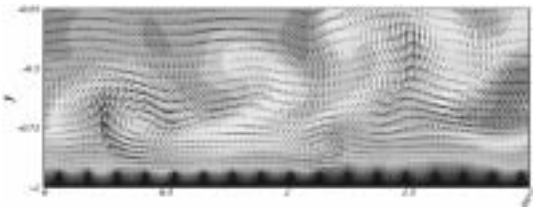

(b)

Fig. 7 Contours of streamwise velocity embedded with the cross-stream velocity vector;
(a) drag increasing spacing of $S^+\sim43$ and
(b) drag reducing spacing of $S^+\sim17$

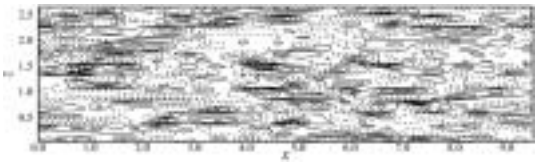

(a) $y^+\sim14$ at the riblet side

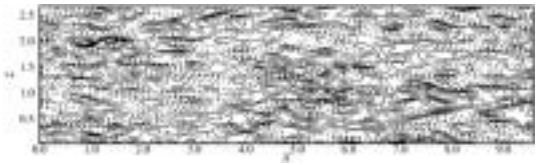

(b) $y^+\sim23.5$ at the riblet side

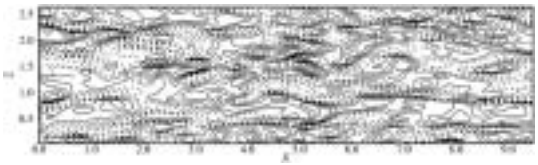

(c) $y^+\sim14$ at the smooth surface

Fig. 8 Low- and high-speed streaks for drag-increasing case $S^+\sim43$

(a) $y^+\sim6.2$ at the riblet side

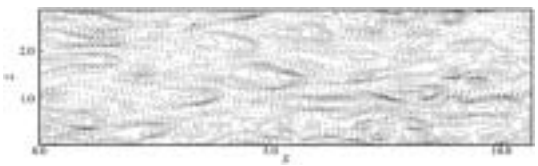

(b) $y^+\sim24$ at the riblet side

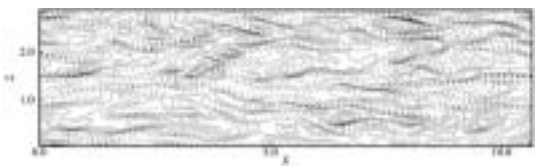

(c) $y^+\sim14$ at the smooth surface

Fig. 9 Low- and high-speed streaks for drag-decreasing case $S^+\sim17$

flow as shown in Fig. 8(c). In the case of drag-reduction case, the valley show much more suppression of the streaks. Bear in mind that the number of riblets in this case is 24 and they are removed from the image in Fig. 9(a) for clarity. Streaks above the riblets tip and above the smooth surface both obtained at elevations where u'_{rms} is maximum are shown in Fig. 9(b) and (c), respectively. They appear very similar suggesting again the riblet with such narrow spacing damp the layer occupying the riblet height with their valleys. Hence, the activity of turbulence above the tips resembles that of smooth surface which means the thickening of the boundary layer.

Spatial average over the x-direction can give a picture of the coherence of events occurring near the riblets. Fig. 10 shows the spatial average of $-\overline{u'v'}$ for drag-increasing (Fig. 10(a)) and reducing case (Fig. 10(b)). It can be distinguished clearly that the riblets play a role in concentrating the generating of Reynolds shear stress to near riblet tips in the drag-increasing case, as shown in Fig. 10(a). The wide spacing, in this case, permits the penetration of small eddies to reside in the valley between riblets. Therefore, it is more likely to find inrushes of fluids from the bottom of the valley to move adhesively to the riblets side-walls and give a jet like flow near the tips as it was shown in Fig. 7(a). Such concentration of Reynolds shear stress diminishes in the drag-reducing case as shown in Fig. 10(b).

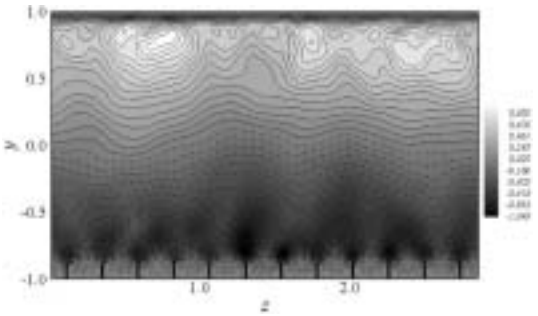

(a) Drag-increasing case ($S^+ \sim 43$)

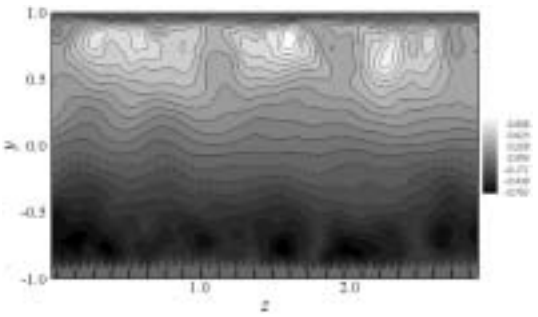

(b) Drag-decreasing case ($S^+ \sim 17$)

Fig. 10 Spatial average of the Reynolds stress $\langle u'v' \rangle$

4. Conclusions

The immersed boundary method (IBM) has shown potential in predicting flow fields over complicated geometries. In an initial stage of testing the performance of IBM in simulating riblets of different shapes, simplified thin rectangular riblets aligned in the streamwise direction are investigated and compared with the experimental results. Good agreement of the present prediction of the drag reduction rates with the experiments despite the larger rates of reduction. The important point in the present study is that the IBM could mimic very thin riblets and predicted well the optimum spacing at which the drag can be minimized.

The present study demonstrates the significant changes in Reynolds stresses as well as the instantaneous fields over the riblets. Larger spacing than the nominal sizes of the quasi-streamwise coherent structures leads to the possibility of penetrating them into the valley between riblets which in turns results in larger drag. The two classes of drag-increasing and drag-decreasing cases are highlighted.

Finer grid system is needed to verify the dependence of the drag calculation on the grid system resolution in order to explain the higher rates obtained in the present study compared with those of the experiments. The present results in general is encouragingly to move in simulating more complicated shapes of riblets aiming at proposing an optimum geometry for maximizing the drag reduction rates.

Acknowledgments

This work was supported by Advanced Ship Engineering Research Center (ASERC), Pusan

National University, through the Korean Science and Engineering Foundation.

References

Bechert, D. W. and Bartenwerfer, M., 1989, "The Viscous Flow on Surfaces with Longitudinal Ribs," *J. Fluid Mech.*, Vol. 206, pp. 105~129.

Bechert, D. W., Bruce, M., Hage, W., Van Der Hoeven, J. G. T. and Hoppe, G., 1997, "Experiments on Drag Reducing Surfaces and Their Optimization with an Adjustable Geometry," *J. Fluid Mech.*, Vol. 338, pp. 59~87.

Bechert, D. W., Bruce, M. and Hage, W., 2000, "Experiments with Three-Dimensional Riblets as an Idealized Model of Shark Skin," *Experiments in Fluids*, Vol. 28, pp. 403~412.

Bruce, M., Bechert, D. W., Van Der Hoeven, J. G. T., Hage, W. and Hoppe, G., 1993, "Experiments with Conventional and with Novel Adjustable Erag-Reducing Surfaces," *In So, R. M. C.; Speziale, C. G.; Launder, B. E. Eds., Near-Wall Turbulent Flows, Elsevier, Amsterdam*, pp. 719~738.

Choi, H., Moin, P. and Kim, J., 1993, "Direct Numerical Simulation of Turbulent Flow over Riblets," *J. Fluid Mech.*, Vol. 255, pp. 503~539.

Choi, K. S., 1989, "Near-Wall Structure of Turbulent Boundary Layer with Riblets," J. Fluid Mech., Vol. 208, pp. 417~458.

Chu, D. C. and Karniadakis, G. E., 1993, "A Direct numerical Simulation of Larminar and Turbulent Flow over Riblet-Mounted Surfaces," *J. Fluid. Mech.*, Vol. 250, pp. 1~42.

El-samni, O. A., Yoon, H. S. and Chun, H. H., 2005, "DNS of Turbulent Flow over thin Rectangular Riblets," *2nd International Symposium on Seawater Drag Reduction, Busan, Korea, 23-26 May 2005*, pp. 517~527.

Goldstein, D., Handler, R. and Sirovich, L., 1995, "Direct Numerical Simulation of Turbulent Flow over a Modeled Riblet-Covered Surface," *J. Fluid. Mech.*, Vol. 302, pp. 333~376.

Goldstein, D., Handler, R. and Sirovich, L., 1995, "Modeling a No-Slip Flow Boundary with an External Force Field," *J. Comput. Phys.*, Vol. 105, pp. 354~366.

Kim, J., Kim, D. and Choi, H., 2001, "An Immersed-Boundary Finite Volume Method for Simulations of Flow in Complex Geometries," *J. Comput. Phys.*, Vol. 171, pp. 132~150.

Kim, J. and Moin, P., 1985, "Application of a Fractional Step Method to Incompressible Navier-Stokes Equations," *J. Comput. Phys.*, Vol. 59, pp. 308~323.

Kim, J., Moin, P. and Moser, R. D., 1987, "Turbulence Statistics in Fully Developed Channel Flow at Low Reynolds Number," *J. Fluid Mech.*, Vol. 177, pp. 133~166.

Saiki, E. M. and Biringen, S., 1996, "Numerical Simulation of a Cylinder in Uniform Flow : Application of a Virtual Boundary Method," *J. Comput. Phys.*, Vol. 123, pp. 450~465.

Stalio, E. and Nobile, E., 2003, "Direct Numerical Simulation of Heat Transfer over Riblets," *Int. J. of Heat and Fluid*, Vol. 24, pp. 356~371.

Suzuki, Y. and Kasagi, N., 1994, "Turbulent Drag Reduction Mechanism Above a Riblet Surface," *AIAA Journal*, Vol. 32, No. 9, pp. 1781~1790.

Vukoslavcevic, P., Wallace, J. M. and Balint, J. L., 1992, "Viscous Drag Reduction Using Streamwise-Aligned Riblets," *AIAA Journal*, Vol. 30, No. 4, 1119~1122.

Walsh, M. J., 1982, "Turbulent Boundary Layer Drag Reduction Using Riblets," *AIAA paper*, pp. 82~169.

Walsh, M. J., 1983, "Riblets as a Viscous Drag Reduction Technique," *AIAA Journal*, Vol. 21, No. 4, pp. 485~486.

Ye, T., Mittal, R., Udaykumar, H. S. and Shyy, W., 1999, "An Accurate Cartesian Grid Method for Viscous Incompressible Flows with Complex Immersed Boundaries," *J. Comput. Phys.*, Vol. 156, pp. 209~240.

Zang, Y., Street, R. L. and Koseff, J. R., 1994, "A Non-staggered Grid, Fractional Step Method for Time-Dependent Incompressible Navier-Stokes Equations in Curvilinear Coordinates," *J. Comput. Phys.*, Vol. 114, pp. 18~33.